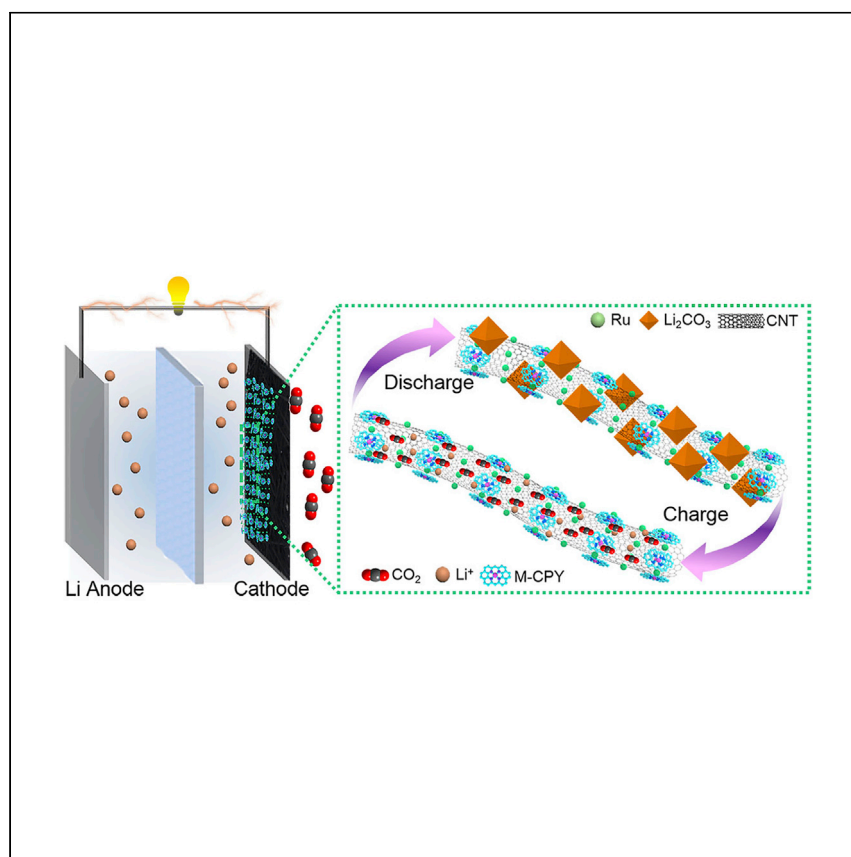**Article**

Single-metal site-embedded conjugated macrocyclic hybrid catalysts enable boosted CO_2 reduction and evolution kinetics in Li-CO_2 batteries

Wang et al. report a series of Ru/M-CPY@CNT hybrid materials assembled from single-metal site-embedded conjugated macrocyclic compounds, Ru nanoparticles, and CNTs. The obtained hybrid materials enable enhanced CO_2 reduction and evolution kinetics in Li-CO_2 batteries.

Jian-Hui Wang, Yu Zhang, Ming Liu, ..., Yifa Chen, Shun-Li Li, Ya-Qian Lan

chyf927821@163.com (Y.C.)
yqlan@njnu.edu.cn,
yqlan@m.scnu.edu.cn (Y.-Q.L.)

Highlights

Ru/M-CPY@CNT with multi-functionality is prepared via a self-assembly method

Ru/Co-CPY@CNT can be applied as efficient cathode catalyst in Li-CO_2 batteries

Ru and Co-CPY show synergistic effect for the discharge/charge process

The CO_2 activation ability of Co-CPY is revealed by DFT calculations

Article

Single-metal site-embedded conjugated macrocyclic hybrid catalysts enable boosted CO_2 reduction and evolution kinetics in Li-CO_2 batteries

Jian-Hui Wang,[1,4] Yu Zhang,[1,4] Ming Liu,[1,4] Guang-Kuo Gao,[1] Wenxin Ji,[3] Cheng Jiang,[1] Xin Huang,[1] Yifa Chen,[1,2,*] Shun-Li Li,[1] and Ya-Qian Lan[1,2,5,*]

SUMMARY

Rechargeable Li-CO_2 batteries, an emerging battery technology to confront the environmental and energy crises, hold promise for CO_2 fixation and energy storage. However, state-of-the-art Li-CO_2 systems generally suffer from sluggish CO_2 reduction/evolution reaction kinetics, and powerful catalysts that can simultaneously facilitate both processes are much desired but largely unrealized. Here, we report a series of Ru, metal-chelated conjugated N_4-macrocyclic metal complex (M-CPY) and carbon nanotube (CNT)-based hybrid materials (Ru/M-CPY@CNT) with the advantages of highly dispersed Ru and M-CPY, high-conductivity, and tunable loadings that can be applied as multi-functional cathode catalysts. Ru/Co-CPY@CNT-2-based cells deliver an ultra-low overpotential (0.84 V) and enable fully reversible discharge/charge with a high specific capacity of 24,740 mAh/g within 2.0–4.5 V at 200 mA/g. It can rapidly discharge/charge for 180 cycles at 500 mA/g, and the CO_2 activation process is intensively investigated by density functional theory (DFT) calculations.

INTRODUCTION

Capture and green conversion of CO_2 into valuable fuels or renewable energy have received much attention and remain a topic of widespread interdisciplinary interest and global activity all around the world because of the yearly increase in CO_2 concentration that is approaching the warning line (450 ppm).[1,2] Since the first introduced primary Li-CO_2 batteries (without O_2),[3] Li-CO_2 batteries, as an innovative energy storage strategy that can simultaneously capture CO_2 and store electrical energy, have attracted tremendous attention because of their high theoretical energy density (1,876 Wh kg^{-1}) compared with Li-ion batteries ($\approx$ 265 Wh kg^{-1}).[4] It has been demonstrated that CO_2 can be used as an energy carrier to store renewable energy in terms of an aprotic Li-CO_2 battery, which operates based on the possible discharge reaction $4Li^+ + 3CO_2 + 4e^- \rightarrow 2Li_2CO_3 + C$.[5–9] Additionally, Li-$CO_2$ batteries are potential power sources for certain scenarios with high CO_2 concentration (e.g., factories or power plants) and even for migration to Mars (96% vol of CO_2 in atmosphere).[10] However, several critical bottlenecks, including the high overpotential, poor rate capacity, low recyclability, and energy density on the device level, have restricted practical applications of this technology, which lies in the design of high-efficiency CO_2 electrodes that enable simultaneous catalysis of the CO_2 reduction reaction (CRR) and CO_2 evolution reaction (CER).[11] Specifically, Li_2CO_3, as a kind of highly insulating discharge product of CRR, is thermodynamically unfavorable, and constant deposition of it will cause the battery to expand, severe cathode or electrolyte instability, CO_2 capture barrier, poor conductivity, or burying of catalysis sites, which generally

require cathode catalysts to facilitate the decomposition process and lower the high charge potential.[12] In addition, significant hurdles in investigation of the CRR process regarding activation of CO_2 or formation of Li_2CO_3 also need to be overcome before Li-CO_2 batteries become a viable option for energy storage.[13]

To date, many cathode catalysts, such as porous carbon-based materials,[14–17] noble metals,[18–21] transition metals or oxides/carbides,[22–25] metal-organic frameworks (MOFs),[26] and covalent organic frameworks (COFs),[27–29] have been explored. Commonly applied cathode catalysts with high performance are mostly based on noble metals such as Ru or Ir, which have been proven to be responsible for the Li_2CO_3 decomposition process in the CER.[7,20,21] Nonetheless, most of them focus on the CER process and generally have a relatively weak effect on the CRR process based on previously reported works, as far as we know. To address this, various strategies, such as hybridization with other metals (e.g., Rh, Co, or Cu),[30–32] metal oxides,[33,34] carbon materials,[20] or COFs,[27] have been proposed to improve performance. However, most hybrid materials still ignore the CO_2 activation process in the CRR, and the mechanism of Li_2CO_3 formation remains unexplored. Therefore, exploration of powerful CRR catalysts that can be combined with noble metals to simultaneously facilitate the CRR and CER processes might be desired to achieve low overpotential, high stability, and excellent cycling performance in Li-CO_2 batteries.

Conjugated macrocyclic compounds with single-metal sites (e.g., porphyrins and phthalocyanines) that can be integrated with a broad choice of metal centers have shown high promise for various applications, such as catalysis, solar batteries, biochemical applications, and energy storage.[35–38] Especially attractive is their potential as CRR catalysts in Li-CO_2 batteries, which have been proven to be beneficial for the CO_2 activation process.[30,39,40] However, several critical challenges, such as the inert crystalline nature, poor conductivity, unexplored CO_2 activation, or Li_2CO_3 decomposition process, have largely restricted their possible application in this field. Therefore, exploration of new conjugated macrocyclic compounds with unique properties or new strategies to address the remaining bottlenecks is much desired. With these considerations, conjugated N_4-macrocyclic ligands (CPYs) come to mind as a prototype for efficient cathode catalysts.[41,42] Compared with the commonly applied porphyrin or phthalocyanine, CPY molecules have a higher conjugated structure that is more conducive to delocalization of electrons around nitrogen, enhancement of electron density, and facilitating electronic delivery between nitrogen and metal.[41] The planar configuration of conjugated CPY makes it a highly delocalized elevation electronic orbit, and it has a better interaction with the substrate through π-π interaction, which can be considered an ideal ligand for metal chelation and subsequent hybridization.[42] Hence, we propose to assemble metal-chelated conjugated N_4-macrocyclic metal complex (M-CPY) and typical metal catalysts like Ru with carbon nanotubes (CNTs) to design a kind of well-dispersed hybrid material. The corresponding considerations are as follows. (1) M-CPY molecules with highly conjugated structure and tremendous transition metal-N_4 (M-N_4) sites might be favorable for the CRR process, including CO_2 activation or the Li_2CO_3 formation process. (2) Ru, a common catalyst for Li-CO_2 batteries, is beneficial for the CER process. (3) CNTs, a kind of conductive substrate with high electrical conductivity, large surface area, abundant channels, and porosity, might provide strong π-π interactions with M-CPY[43,44] or serve as a desired platform for Ru loading to realize high electrical conductivity and fast electron transfer. (4) The synergistic integration of Ru, M-CPY, and CNTs will presumably create a powerful catalysis system in which Ru is beneficial for discharge product decomposition, M-CPY favors CO_2
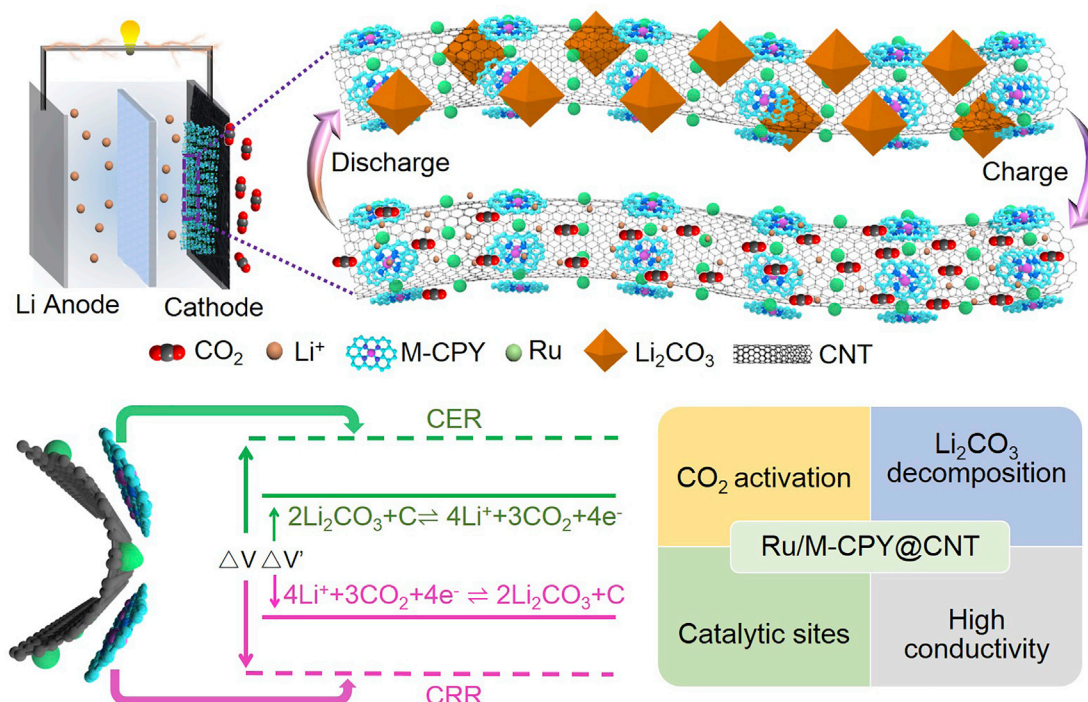
Figure 1. The schematic representation of Ru/M-CPY@CNT and their advantages as cathode catalysts in Li-CO$_2$ battery

activation, and CNTs can provide electrical conductivity, allowing the CRR/CER kinetics in the hybrid materials (Figure 1). From the above, we deduce that the hybrid materials M-CPY, Ru, and CNTs will probably be promising candidates to enhance the performance of Li-CO$_2$ batteries, but exploration of these types of materials has rarely been reported.

Here we report a series of Ru/M-CPY@CNT (M = Co, Mn, Zn, and Ni) hybrid materials and successfully apply them as efficient cathode catalysts in Li-CO$_2$ batteries (Figure 1). In the hybrid materials, M-CPY and Ru nanoparticles (NPs) can be loaded uniformly loaded on CNTs with tunable loading and morphology. The obtained hybrid materials possess the characteristics of uniformly dispersed morphology of Ru NPs and M-CPY and high electrical conductivity. Ru/Co-CPY@CNT-2-based batteries deliver an ultra-low overpotential (0.84 V) with a high discharge platform of 3.06 V and low charge platform of 3.90 V, which is best among crystalline materials and superior to most Ru-based catalysts. It displays a fully reversible discharge/charge process with a high specific capacity of 24,740 mAh/g within 2.0–4.5 V at 200 mA/g. It can be discharged and charged rapidly for 180 cycles at 500 mA/g. The CO$_2$ activation pathways of different conjugated macrocyclic compounds (e.g., CPY, porphyrin [TPP], and phthalocyanine [Pc]) with M-N$_4$ sites were investigated systematically using density functional theory (DFT) calculations, which revealed the superior role of CPY in high-performance Li-CO$_2$ batteries.

RESULTS

Characterization of Ru/M-CPY@CNT hybrid materials

The CPY molecule with high conjugation structure is prepared by thermal polymerization of 2,9-dimethyl-1,10-phenanthroline and 2,9-dichloro-1,10-phenanthroline under an argon atmosphere.[45] To prove successful synthesis of the molecule, elemental analyses of the atom percentage were conducted, and the results (C, 80.74; H, 4.26; N,
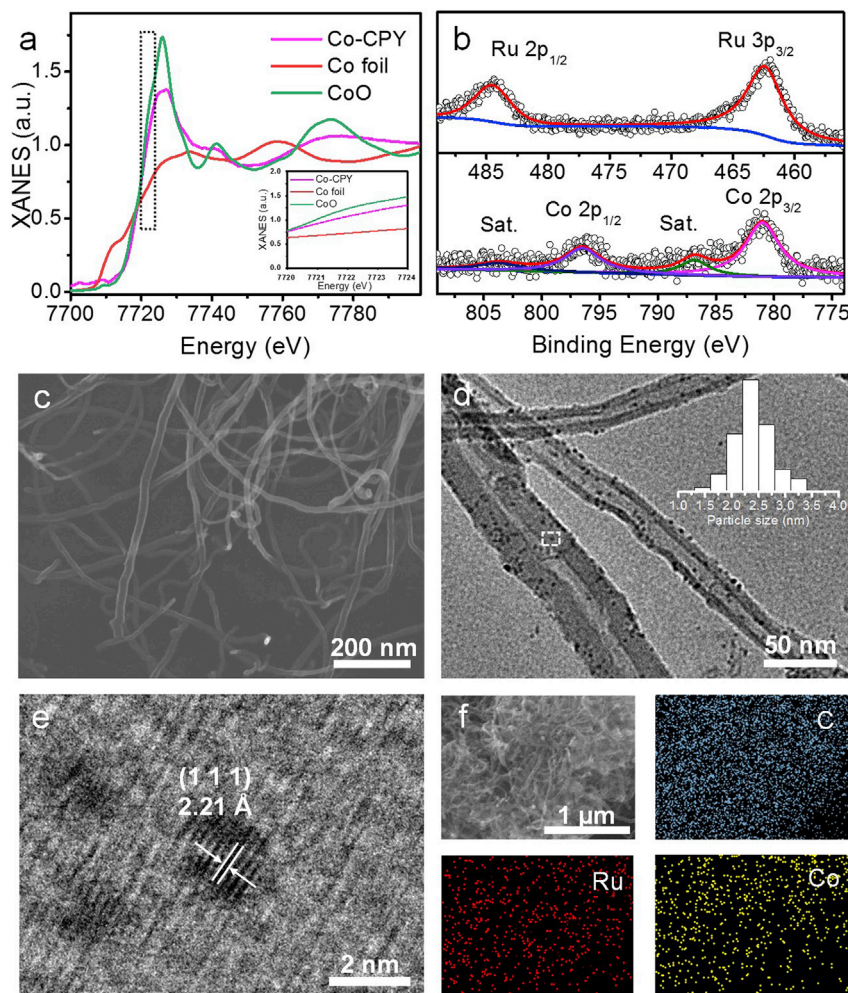
Figure 2. Characterization of Ru/Co-CPY@CNT-2

(A) XANES spectra at the Co K-edge of Co foil, CoO, and Co-CPY.

(B) XPS analyses of Co and Ru for Ru/Co-CPY@CNT-2.

(C) SEM image of Ru/Co-CPY@CNT-2.

(D) TEM image of Ru/Co-CPY@CNT-2.

(E) Enlarged image of the circled place in (D).

(F) Elemental mapping images of Ru/Co-CPY@CNT-2.

14.99) match well with the calculated ones (C, 81.2; H, 4.2; N, 14.6). Specifically, the N_4 site in the middle of the CPY molecule can be modified with a variety of transition metals. Taking Co-CPY as an example, Co has been proven to be doped in the N_4 center after 24-h reflux (160°C) under an Ar atmosphere, as shown by mass spectrometry (MS) (for details, see Supplemental experimental procedures).[42] X-ray absorption near edge structure (XANES) and extended X-ray absorption fine structure (EXAFS) spectra confirmed the structure of Co-CPY, especially the coordination mode of Co (Figure 2A; Figure S1; Table S1). According to the normalized XANES spectra of Co-CPY and several reference materials, including CoO and Co foil, as shown in Figure 2A and the inset image, the absorption edge position of Co-CPY is located similarly as that of CoO, indicating that the Co species in Co-CPY is presented as Co (II).[46–48] In addition, as shown in Figure S1A, the Fourier-transformed EXAFS spectrum of Co-CPY shows a main peak at ~1.44 Å that can be assigned to the Co-N bond. The peak related to the Co-Co bond at ~2.2 Å is absent. According to the EXAFS fitting results, the Co

atom coordinates with N atoms and the coordination number (3.9) are close to 4, which supports the existence of Co-N$_4$ sites in Co-CPY (Figure S1B; Table S1).[49] It can be seen from Fourier transform infrared (FTIR) spectroscopy that the original characteristic peak of the N-H bond (3,032 cm^{-1}) disappears after the metal doping coupling with the maintenance of characteristic peak for C = N (1,629 cm^{-1}), which proves successful doping of Co ions and remained inert structure of CPY (Figure S2).[50] Moreover, M-CPY (M = Zn, Mn, and Ni) with different metal centers was synthesized following similar procedures as for Co-CPY and characterized by FTIR spectroscopy (Figure S2). Based on the successful syntheses of M-CPY, a series of Ru/M-CPY@CNT was prepared using a polyol reduction method to apply M-CPY, CNTs, and RuCl$_3$ · xH$_2$O as the raw materials, during which RuCl$_3$ · xH$_2$O can be reduced to Ru NPs and co-assembly with M-CPY to generate hybrid materials. This strategy also facilitates tuning the composition. For example, Ru/Co-CPY@CNT-x (x = 1–3) with different compositions was obtained by tuning the ratios of precursors for further characterization and battery tests (for details, see Supplemental experimental procedures).

To evaluate the basic properties of the hybrid materials, a series of characterizations, including phase, composition, and morphology tests, were been performed. Powder X-ray diffraction (PXRD) tests show that the patterns of Ru/Co-CPY@CNT-x (x = 1–3) are consistent with that of pure CNTs (Figure S3). X-ray photoelectron spectroscopy (XPS) confirms that Ru(III) is reduced successfully to Ru with the characteristic core level peaks at 462.4 eV for Ru 3p$_{3/2}$ and 484.6 eV for Ru 3p$_{1/2}$ (Figure 2B).[27] In contrast, Co has retained a bivalent valance with the relative characteristic core level peaks of 781.0 eV for Co 2p$_{3/2}$ and 796.5 eV for Co 2p$_{1/2}$ (Figure 2B). To characterize the morphology, transmission electron microscopy (TEM) and scanning electron microscopy (SEM) tests were performed. Taking Ru/Co-CPY@CNT-2 as an example, the surfaces of CNTs are still smooth after loading of Ru and Co-CPY, and their diameters (20–50 nm) remain almost unchanged compared with that of bare CNTs (Figure 2C; Figure S4). As expected, CNTs with hollow tube morphology are uniformly modified with Ru NPs (average size, 2.38 nm), as seen in the TEM image (Figure 2D). When tuning the added amount of precursors, the particle sizes of uniformly distributed Ru NPs in Ru/Co-CPY@CNT-x (x = 1–3) are slightly different, with a volcano shape in size trend from Ru/Co-CPY@CNT-1 to Ru/Co-CPY@CNT-3 (Figure 2D; Figures S5 and S6). For example, the average particle size of Ru NPs in Ru/Co-CPY@CNT-1 material is 1.71 nm and increases to 2.38 nm for Ru/Co-CPY@CNT-3 but is reduced to 2.08 nm for Ru/Co-CPY@CNT-2 (Figures S5 and S6). The distribution of Ru NPs becomes denser from Ru/Co-CPY@CNT-1 to Ru/Co-CPY@CNT-3, matching well the possible results from the increased amount of RuCl$_3$ · xH$_2$O in the precursors. These results are supported by the XPS tests, in which the atom mole ratios of Co and Ru in Ru/Co-CPY@CNT-1, Ru/Co-CPY@CNT-2, and Ru/Co-CPY@CNT-3 are calculated to be 0.67, 0.53, and 0.34, respectively (Table S2).

In addition, the high-resolution TEM (HR-TEM) image of Ru/Co-CPY@CNT-2 shows that the interval of 2.21 Å belongs to the (111) lattice spacing of Ru (PDF #88-2333) (Figure 2E). Elemental mapping images reveal that Co and Ru are distributed uniformly on CNTs, indicating high dispersion of Ru NPs and Co-CPY in the hybrid material (Figure 2F).[51] As mentioned above, Co-CPY with a highly conjugated structure might possess strong π-π interactions with highly delocalized π electron orbital groups in CNTs. To prove the possible interaction between Co-CPY and CNTs, Raman tests were carried out and analyzed. Interestingly, the test results show that the peak positions of the G band for CNTs are shifted from 1,576.64 cm^{-1} to 1,581.31 cm^{-1}, which verifies the existing strong interaction in Ru/Co-CPY@CNT-2 (Figure S7).[52]

To extend the diversity of the hybrid materials, Ru/M-CPY@CNT (M = Zn, Mn, and Ni) was synthesized following similar procedures as those for Ru/Co-CPY@CNT-2, but Co-CPY was replaced with Zn-CPY, Mn-CPY, and Ni-CPY. PXRD tests show that they present similar peaks as Ru/Co-CPY@CNT-2 (Figure S8). As seen in TEM images, Ru NPs with similar particle sizes ($\sim$2.50 nm) are distributed uniformly on CNTs in these extended hybrid materials (Figure S9). XPS analyses confirm the existence of Ru, as shown by the detected similar peak positions of Ru $3p_{3/2}$ and Ru $3p_{1/2}$ compared with Ru/Co-CPY@CNT-2 (Figures S10–S12). Moreover, Ru/Zn-CPY@CNT presents a retained bivalent valance with the characteristic peaks at 1,022.2 eV for Zn $2p_{3/2}$ and 1,045.4 eV for Zn $2p_{1/2}$ (Figure S10). Similarly, Ru/Ni-CPY@CNT and Ru/Mn-CPY@CNT exhibit bivalent characteristic peaks (Figures S11 and S12). The obtained M-CPY (M = Co, Zn, Mn, and Ni)-based hybrid materials with advantages like tunable composition, uniformly distributed morphology, and accessible metal sites set a fundamental basis for further Li-CO_2 battery applications.

Electrochemical performance of Li-CO_2 batteries

To test the performance of Li-CO_2 batteries, a mixture of cathode material (90 wt %) and polyvinylidene fluoride (PVDF; 10 wt %) is ground with a certain volume of N-methylpyrrolidone. The obtained suspension is then dropped onto carbon paper, and the cathodes are dried at 100°C under a vacuum for 12 h. The mass loading of the active material is controlled to be 0.1–0.15 mg cm^{-2} with the gravimetric current density and capacity normalized to the total cathode material. 1.0 M LITFSI in TEGDME is employed as the electrolyte. All of the preparation processes of Li-CO_2 batteries are performed in an argon-filled glovebox with water and oxygen contents below 0.1 ppm.

As mentioned above, Ru/Co-CPY@CNT-x (x = 1–3) was synthesized successfully with well-controlled morphology and composition. To determine the effect of different compositions on the Li-CO_2 system, the initial battery properties of these samples as cathode catalysts were evaluated. Figure 3A shows the discharge/charge curves of relative electrodes cycled at a constant current density of 100 mA/g with a limited capacity of 1,000 mAh/g. Ru/Co-CPY@CNT-2 (discharged potential, 3.06 V; charged potential, 3.90 V) shows much better catalytic activity Ru/Co-CPY@CNT-1 (2.91 V and 4.01 V) and Ru/Co-CPY@CNT-3 (2.88 V and 4.07 V). At the same time, its overpotential for the first cycle is only 0.84 V, which is best among crystalline materials and superior to most Ru-based materials (Table S3). To further demonstrate the functions of relative components in the hybrid materials, Ru@CNT and Co-CPY@CNT, a physical mixture of Co-CPY and Ru@CNT, were synthesized and characterized as contrast samples (Figure S13). The discharge/charge curves of relative electrodes cycled at a constant current density of 100 mA/g with a limited capacity of 1,000 mAh/g were analyzed. In the absence of Co-CPY, the discharge voltage platform of the first cycle for Ru@CNT is as low as 2.69 V, and the charge voltage is 4.15 V, which confirms the previous hypothesis that Ru is more beneficial for the CER process to reduce the charge platform but still lacks the catalysis ability for the CRR process (Figure S14).[7,18] For Co-CPY@CNT, the discharge voltage platform of the first cycle is 2.95 V, and the charge voltage is 4.40 V, suggesting a viral role of Co-CPY in enhancing the discharge platform (Figure S15). The performance of the physical mixture of Co-CPY and Ru@CNT under the same input ratio of Ru/Co-CPY@CNT-2 at a current density of 100 mA/g with a limited capacity of 1,000 mAh/g was also tested. Specifically, it has a discharge platform of 2.89 V and a discharge platform of 4.24 V for the first cycle (Figure S16). After 20 cycles, the discharge platform decreases to 2.68 V, and the charge platform is as high as 4.28 V, which is inferior to Ru/Co-CPY@CNT-2 (discharge platform, 2.81 V and charge platform, 3.91 V)
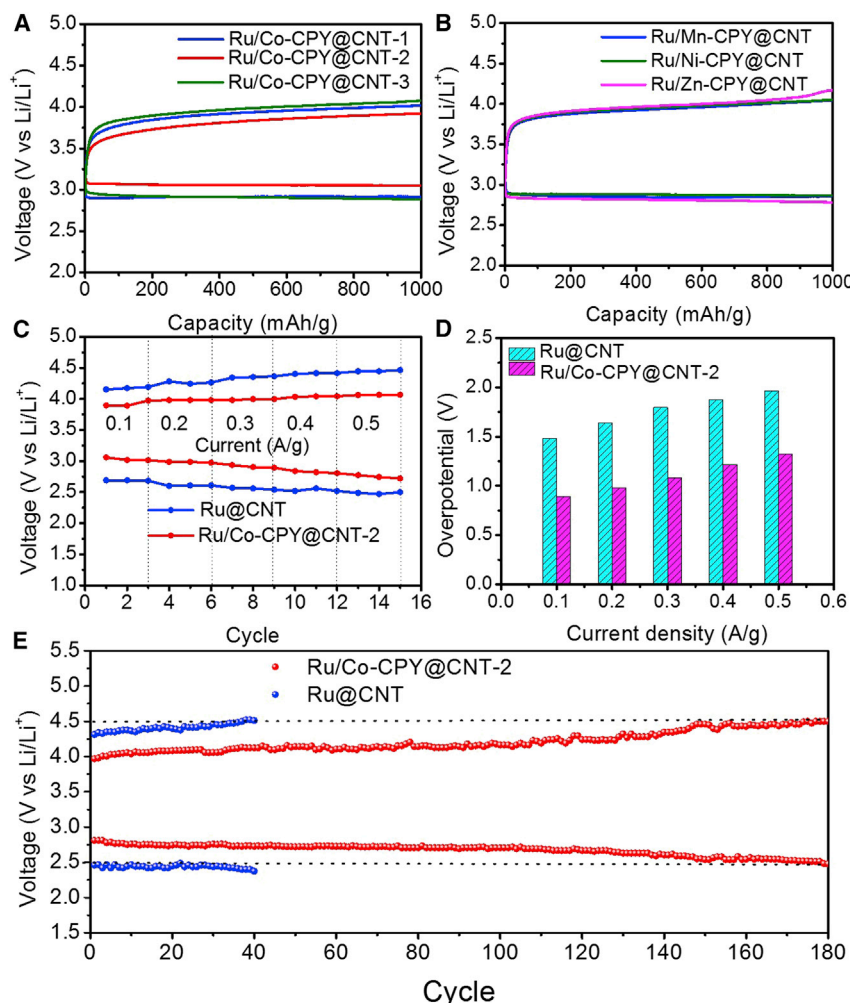
Figure 3. The electrochemical performance of a Li-CO$_2$ battery with Ru/Co-CPY@CNT-x (x = 1–3) and Ru/M-CPY@CNT (M = Mn, Zn, and Ni) as the cathode catalysts

(A) The discharge/charge cycling curves of the first cycle of Ru/Co-CPY@CNT-1, Ru/Co-CPY@CNT-2, and Ru/Co-CPY@CNT-3 with a limited capacity of 1,000 mAh/g at 100 mA/g.

(B) The discharge/charge curves of the first1st cycle of Ru/Zn-CPY@CNT, Ru/Ni-CPY@CNT, and Ru/Mn-CPY@CNT with a limited capacity of 1,000 mAh/g at 100 mA/g.

(C) Rate performance within a limiting capacity of Ru/Co-CPY@CNT-2 and Ru@CNT of 1,000 mAh/g at various current densities.

(D) The discharge/charge potentials of different cathodes at various current densities of 100 mA/g, 200 mA/g, 300 mA/g, 400 mA/g, and 500 mA/g.

(E) Long-term cycling curves of Ru/Co-CPY@CNT-2 and Ru@CNT cathode catalysts at 500 mA/g.

(Figure S17). These results support the superiority of Ru/Co-CPY@CNT-2, in which the integrated Ru and Co-CPY with uniformly distributed morphology on CNTs might have synergistic effect on improvement of Li-CO$_2$ battery performance.

Ru/M-CPY@CNT (M = Zn, Ni, Mn) with different kinds of M-CPY were also prepared as cathode catalysts to evaluate the effect of varied transition metal sites on battery performance. The discharge/charge curves of the first cycle for Ru/Zn-CPY@CNT, Ru/Ni-CPY@CNT, and Ru/Mn-CPY@CNT with a limited capacity of 1,000 mAh/g at 100 mA/g were tested (Figure 3B). Ru/Ni-CPY@CNT and Ru/Mn-CPY@CNT present a similar discharge voltage at ∼2.86 V and charge voltage at ∼4.05 V. After 20 cycles,

their discharge platforms decay to ~2.7 V, and the charge platforms reach up to ~4.23 V (Figures S18 and S19). In contrast, Ru/Zn-CPY@CNT presents poorer performance in discharge/charge platforms for the first cycle (~2.78 V and ~4.17 V) and 20 cycles (~2.68 V and ~4.28 V) (Figure S20). Based on the experimental results, we can reach the conclusion that M-CPY based on Mn, Ni, or Zn has CO_2 activation ability to some extent but is still limited by poor cycling stability compared with Co-CPY.

In general, the severe polarization in Li-CO_2 batteries might result in a large discharge/charge overpotential, which might be caused by the high energy barrier for Li_2CO_3 decomposition or poor electrode kinetics because of sluggish diffusion of reactants (e.g., CO_2 and Li ions). The hybrid materials that can integrate Ru and Co-CPY with uniformly distributed morphology on CNTs (a kind of conductive substrate with a large surface area, abundant channels, and porosity) would be desired cathode catalysts in which CO_2 and Li ions can be channeled to catalytic sites, largely facilitating the kinetics during battery discharge/charge. To confirm this, the internal resistance of Ru@CNT- and Ru/Co-CPY@CNT-2-based Li-CO_2 batteries was measured by EIS analyses, and the calculated results show low EIS values for Ru@CNT-based (22 Ω) and Ru/Co-CPY@CNT-2-based (17 Ω) Li-CO_2 batteries (Figure S21). One positive outcome of the enhanced battery kinetics is an improvement of rate performance; Li-CO_2 batteries invariably display disastrously poor rate performance because of the sluggish kinetics of the discharge/charge reactions. To prove this, the rate performance was evaluated by the end discharge/charge voltage of the batteries at various current densities (0.1–0.5 A g^{-1}) within a limiting capacity of 1,000 mAh/g (Figure 3C). Specifically, the Ru/Co-CPY@CNT-2 cathode exhibits superior rate performance with a small decrease in discharge potential (3.06–2.72 V) and slight increase in charge potential (from 3.9 to 4.07 V) among current densities from 0.1 to 0.5 A g^{-1}. In contrast, the Ru@CNT cathode shows large decay of the discharge potential (from 2.69 to 2.49 V) and apparent enhancement of the charge potential (from 4.15 to 4.45 V) (Figure 3C). The corresponding battery overpotentials at various rates are summarized in Figure 3D. The battery performance of Ru/Co-CPY@CNT-2 is much better than that of Ru@CNT at the same current density (Figures S22–S25). Specifically, the battery cycling tests of Ru/Co-CPY@CNT-2, examined at high current densities of 500 mA/g with a limited capacity of 1,000 mAh/g, display long-term stable performance during 180 cycles at 500 mA/g (Figure 3E). At the same time, only the redox current exists under a CO_2 atmosphere, which proves that CO_2 is the active substance in the cyclic voltammetry (CV) test (Figure S26). These results show that the synergistic effect between Co-CPY and the Ru catalyst can efficiently narrow down the overpotential and enhance the battery kinetics, allowing the battery to run longer cycles and endure higher current densities.

The deep discharge/charge profiles of Li-CO_2 batteries applying Ru/Co-CPY@CNT-2, Ru@CNT, and Co-CPY@CNT as cathode catalysts at 200 mA/g from 2.0–5.0 V versus Li/Li$^+$ are presented in Figure 4A. It should be noted that Ru/Co-CPY@CNT-2 and Ru@CNT batteries are reversible under a deep discharge state and could fully recharge after the deep discharge process. Ru/Co-CPY@CNT-2 (24,740 mAh/g) displays a specific capacity superior to Co-CPY@CNT (12,833 mAh/g) and Ru@CNT (15,579 mAh/g), suggesting a synergistic effect of the two components in the hybrid material. The high starting discharge platforms for Ru/Co-CPY@CNT-2 (3.01 V) and Co-CPY@CNT (2.91 V) imply a function of Co-CPY with Co-N_4 sites that can effectively facilitate the CRR process (Figure 4A).

A powerful Li-CO_2 cathode catalyst must perform functions such as adsorption/enrichment of CO_2, restricting deposition of Li_2CO_3, and catalyzing decomposition
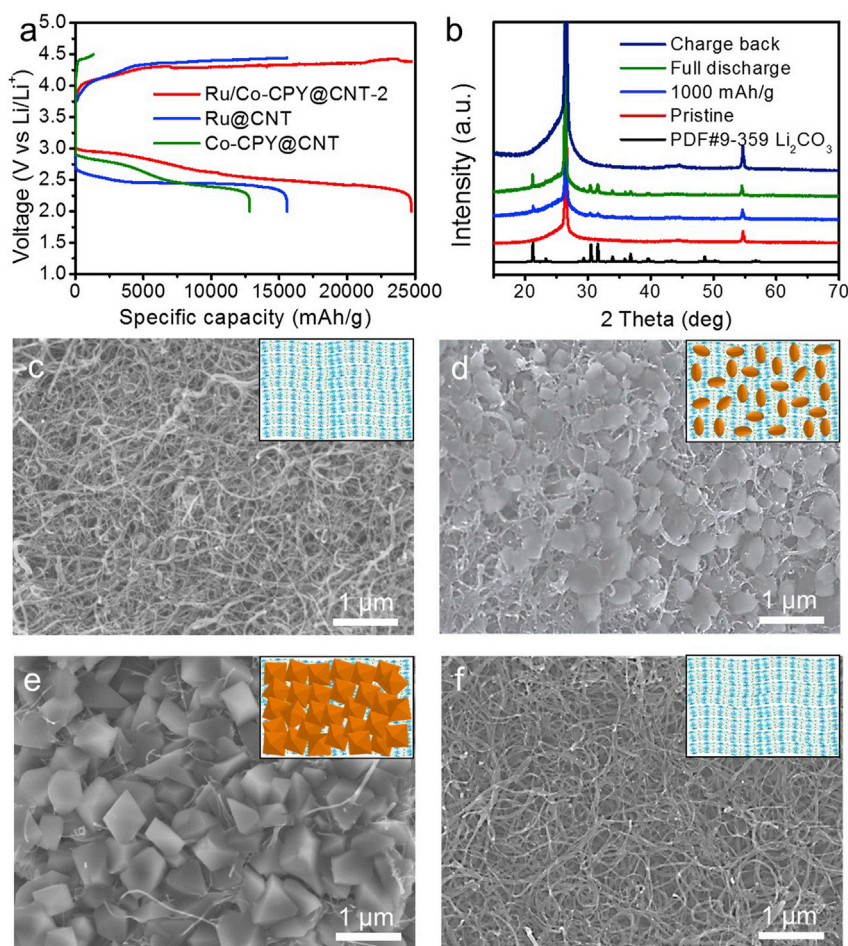
Figure 4. Product characterization of battery reactions

(A) Discharge/charge curves of Ru/Co-CPY@CNT-2-, Ru@CNT-, and Co-CPY@CNT-based electrodes with a limited capacity of 1,000 mAh/g at 200 mA/g and voltage range of 2.0–4.5 V versus Li/Li$^+$.

(B) PXRD patterns of the Ru/Co-CPY@CNT-2-based electrode at different stages.

(C) SEM image of the Ru/Co-CPY@CNT-2-based electrode.

(D) SEM image of discharge of 1,000 mAh/g at 200 mA/g.

(E) SEM image of full discharge.

(F) SEM image of charge back.

of Li$_2$CO$_3$.[27] The poor stability and performance of Li-CO$_2$ batteries are caused mainly by incomplete decomposition of Li$_2$CO$_3$ during the charge process, which might lead to passivation of the cathode surface and decay of battery performance. To investigate the formation and decomposition processes of Li$_2$CO$_3$, the discharge products of Ru/Co-CPY@CNT-2 at different stages in a discharge/charge cycle at 200 mA/g with a voltage range of 2.0–4.5 V versus Li/Li$^+$ were characterized. Specifically, four stages—the pristine state, discharge to 1,000 mAh/g, full discharge, and recharge —during the discharge/charge cycle were selected as desired examples. PXRD tests were performed to characterize the phase changes in the four stages (Figure 4B). At the stage of discharge to 1,000 mAh/g, new peaks that are ascribed to Li$_2$CO$_3$ crystals (PDF 9-359) emerge compared with the pristine one, suggesting that crystalline Li$_2$CO$_3$ is the main discharge product of the batteries. After reaching the full discharge stage starting from 1,000 mAh/g, the peak intensity of Li$_2$CO$_3$ increases (Figure 4B). When the discharged battery is fully charged, the PXRD results

show that the crystallization peaks of Li_2CO_3 have disappeared completely, implying a fully reversible discharge/charge cycle for the battery system (Figure 4B).

To further support the phase change as verified in the PXRD tests, SEM tests were also conducted to reveal the morphology of the generated Li_2CO_3. At the stage of discharge to 1,000 mAh/g, small Li_2CO_3 NPs with a size of $\sim$360 nm are generated on the surface of the Ru/Co-CPY@CNT-2-based cathode compared with the pristine stage (Figures 4C and 4D). After reaching the full discharge stage, Li_2CO_3 NPs grow to produce a kind of octahedral nanocrystals ($\sim$1 μm) that cover most of the surface (Figure 4E). When it is fully charged, Li_2CO_3 NPs disappear, and the stage is consistent with that before discharge, as shown by the SEM image, proving the fully reversible discharge/charge cycle for the battery system (Figure 4F). To validate the functions of Ru and Co-CPY for Li_2CO_3 decomposition, Ru@CNT and Co-CPY@CNT were been evaluated. For Ru@CNT, Li_2CO_3 with nanosheet morphology covers the surface of the CNTs when it is fully discharged, and the electrode can return to its pristine state (Figure S27). However, for Co-CPY@CNT, the produced Li_2CO_3 is distributed unevenly on CNTs in the fully discharged state, and it cannot return to the pristine state during the charge process (Figure S28). Raman and XPS tests were performed before and after charge and discharge. According to the XPS spectra shown in Figure 2B, the Ru and Co signals of the pristine cathode exist and are consistent with the as-synthesized Ru/Co-CPY@CNT-2. Because of formation of Li_2CO_3 on the cathode surface during the discharge process, the Ru and Co signals of the cathode disappear after discharge and can be detected again after the charge process, indicating that there is no obvious metal state change of the cathode catalyst during battery reactions (Figures S29A–S29C). The Raman spectra of cathodes at different states, as shown in Figure S29D, also show the peak of Li_2CO_3 around 1,005 cm^{-1} after discharge, and it disappears after battery recharge, suggesting a reversible discharge-charge processes of the proposed battery. To further confirm full reversibility of the Ru/Co-CPY@CNT-2-based Li-CO_2 battery, *in situ* differential electrochemical MS (DEMS) was performed to monitor the gas evolution during the charge process (Figure S30). The DEMS spectra show that the cell releases CO_2 upon the charge process without any trace of O_2. The charge-to-mass ratio during the charge process is 4.09e^-/3CO_2, which is close to the theoretical value of 4e^-/3CO_2, implying that the process is ascribed to the reversible reaction $4Li^+ + 3CO_2 + 4e^- \rightarrow 2Li_2CO_3 + C$.

To prove the superiority of Co-CPY, Co-TPP and Co-Pc molecules with similar Co-N_4 sites were selected to replace Co-CPY and investigated. The properties of the Ru/Co-Pc@CNT and Ru/Co-TPP@CNT materials were tested under similar conditions and are shown in Figures S31 and S32. The discharge/charge curves of relative electrodes cycled at a constant current density of 100 mA/g with a limited capacity of 1,000 mAh/g show that the battery performance of Ru/Co-Pc@CNT (discharged potential, 2.87 V; charged potential, 4.10 V) and Ru/Co-TPP@CNT (2.78 V and 4.08 V) are inferior to Ru/Co-CPY@CNT-2. In addition, CNTs as a contrast sample were also be tested and exhibited no catalytic activity (Figure S33).

DFT calculations

Based on the results above, Co-CPY plays a positive role in activation and interaction of CO_2 and contributes to the CRR process to improve the performance of Li-CO_2 batteries. Co-CPY-based hybrid materials have higher performance compared with other conjugated macrocyclic compounds with Co-N_4 sites. To obtain further insight into the relationship of geometry, electronic structure, and activity, DFT calculations were performed to investigate the vital role of Co-N_4 sites in reduction of CO_2 in different structures. First, the interaction between conjugated macrocyclic compounds and
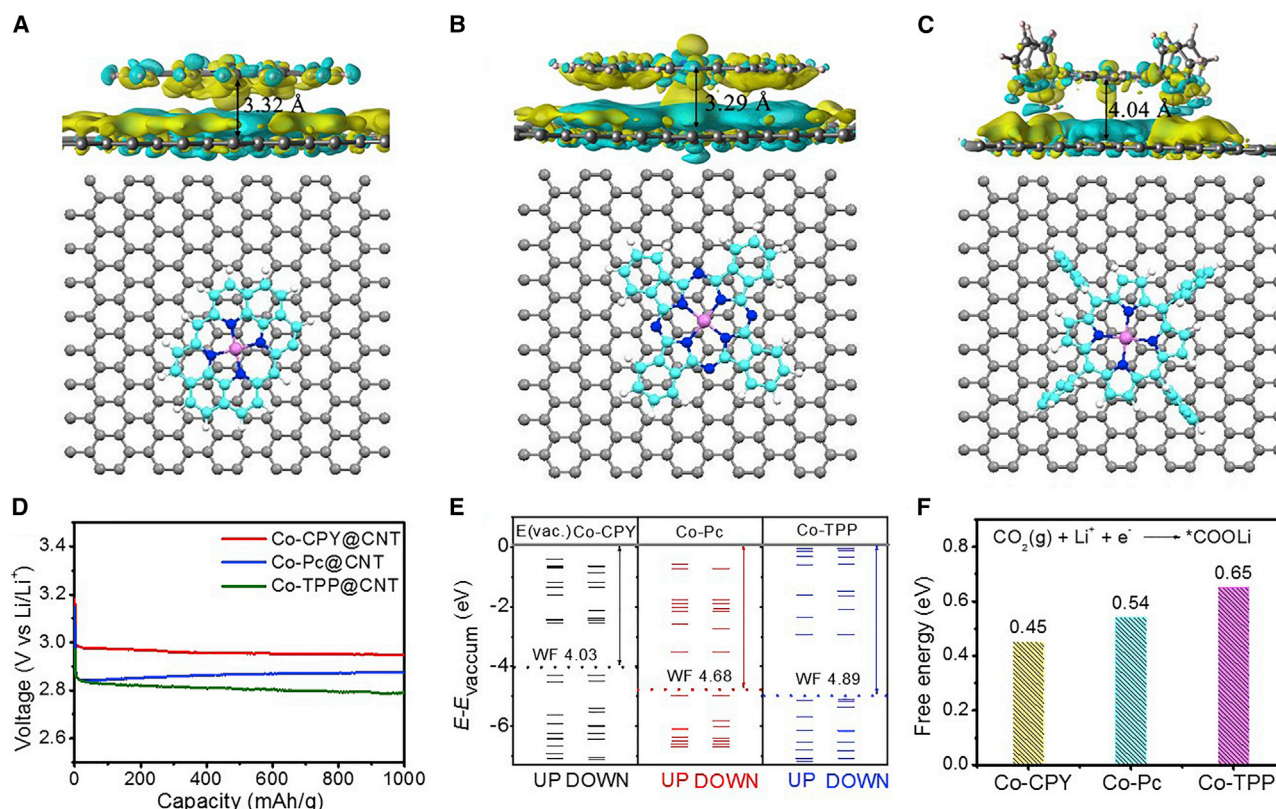
Figure 5. The results of the DFT calculations

(A–C) DFT-optimized structures of Co-CPY@CNT, Co-Pc@CNT, and Co-TPP@CNT (top, side-view image; bottom, top-view image).

(D) The discharge cycling curves of the first cycle of Co-CPY@CNT, Co-Pc@CNT, and Co-TPP@CNT with a limited capacity of 1,000 mAh/g at 100 mA/g.

(E) Electronic structure diagram of Co-CPY, Co-Pc, and Co-TPP.

(F) The free energy of Co-CPY, Co-Pc, and Co-TPP to form *COOLi.

CNTs, which reflects the electron transport mechanism, is investigated by periodic calculations. Although CNTs present curved surface structures, the interacting area can be considered a molecule adsorbed on a flat carbon surface because the diameter of the CNTs (20–50 nm) is much larger than the sizes of the conjugated macrocyclic compounds (6.5–16.5 Å). The CNTs used in the experiments are approximated as a monolayer of graphene (GR), which has commonly been adopted in previous studies.[53] Figures 5A–5C illustrate the optimized hybridized structures, and it can been seen that the planes of Co-CPY and Co-Pc are parallel to the GR surface, forming heterostructures with typical van der Waals distances of 3.32 Å and 3.29 Å, respectively. Consequently, the injected electrons on CNTs can be directly transferred to metal sites by the strong π-π interaction between Co-CPY, Co-Pc, and CNTs. In contrast, the distance between Co-TPP and GR (4.04 Å) is longer than Co-CPY and Co-Pc because of the steric effect by the benzene groups on the edges, suggesting that the transport rate between CNTs and Co-TPP can be much slower compared with the other two.

As the electrons are transferred to the reactive metal sites, the CRR can proceed effectively. To evaluate the activity and performance of the three catalysts, the electronic structures and the free energy change were calculated and are shown in Figures 5E and 5F. With respect to the vacuum level, the energy levels of Co-CPY are higher than those of Co-Pc and Co-TPP, and the work functions of them are 4.03 eV (Co-CPY), 4.68 eV (Co-Pc), and 4.89 eV (Co-TPP) (Figure 5E). The results indicate

that Co-CPY has the strongest electron affinity among them and that the reduction potential of Co^{3+}/Co^{2+} can be smaller than those of the other two. The high activity of Co-CPY can also be proven by activation of CO_2 molecules and the free energy difference between $CO_2(g)$ + Li^+ and *COOLi. Generally, adsorption and activation of CO_2 molecules serve as the first and essential step for the reduction reaction, whereas all three conjugated macrocyclic compounds present weak interactions with the inert gas molecule in the neutral states. Under charged conditions, the three catalysts show different abilities for the activation process. Co-CPY requires 0.4 e^- for transformation from physical adsorption to chemical adsorption with a bent O = C = O structure, whereas the other two catalysts need more electrons of 0.7 e^- (Co-Pc) and 0.8 e^- (Co-TPP) (Figure S34). Similarly, the free energy diagrams of *COOLi generated by activation of CO_2 in the system also prove that the activity of Co-CPY (0.45 eV) is higher than those of the other two, with free energy of Co-Pc (0.54 eV) and Co-TPP (0.65 eV) (Figure 5F). The calculation results agree with the experimental observations that Co-CPY@CNT (2.95 V) has better performance than Co-Pc@CNT (2.88 V) and Co-TPP@CNT (2.78 V) (Figure 5D).

DISCUSSION

We successfully prepared a series of Ru/M-CPY@CNT (M = Co, Mn, Zn, and Ni) hybrid materials through assembly of Ru, M-CPY, and CNTs. In the hybrid materials, M-CPY and Ru NPs can be loaded uniformly on CNTs with tunable loading and can be applied successfully as efficient cathode catalysts in high-performance Li-CO$_2$ batteries. The Ru/Co-CPY@CNT-2-based cell delivers an ultra-low overpotential (0.84 V) with a high discharge platform of 3.06 V and low charge platform of 3.90 V, which is best among crystalline materials and superior to most Ru-based catalysts. It has a fully reversible discharge/charge process with a high specific capacity of 24,740 mAh/g within 2.0–4.5 V at 200 mA/g. The Ru/Co-CPY@CNT-2-based Li-CO$_2$ battery is durable in a higher-stress test at current densities from 100–500 mA/g and can be discharged and charged rapidly for 180 cycles at 500 mA/g. The CO_2 activation pathways of different conjugated macrocyclic compounds with Co-N$_4$ sites were investigated systematically using DFT calculations, which confirmed the superior role of Co-CPY in high-performance Li-CO$_2$ batteries. This work paves the way for exploring conjugated macrocyclic compounds as powerful cathode catalysts for high-performance Li-CO$_2$ batteries.

EXPERIMENTAL PROCEDURES

Resource availability

Lead contact
Further information and requests for resources and reagents should be directed to and will be fulfilled by the lead contact, Ya-Qian Lan (yqlan@njnu.edu.cn; yqlan@m.scnu.edu.cn).

Materials availability
This study did not generate new unique reagents.

Data and code availability
The authors declare that the data supporting the findings of this study are available within the article and the Supplemental information. All other data and codes are available from the lead contact upon reasonable request.

General procedures
Full descriptions of all synthesis, characterization, and electrochemical measurements can be found in the Supplemental experimental procedures.

REFERENCES

1. Marcott, S.A., Bauska, T.K., Buizert, C., Steig, E.J., Rosen, J.L., Cuffey, K.M., Fudge, T.J., Severinghaus, J.P., Ahn, J., Kalk, M.L., et al. (2014). Centennial-scale changes in the global carbon cycle during the last deglaciation. Nature 514, 616–619.

2. Nehrbass-Ahles, C., Shin, J., Schmitt, J., Bereiter, B., Joos, F., Schilt, A., Schmidely, L., Silva, L., Teste, G., Grilli, R., et al. (2020). Abrupt CO_2 release to the atmosphere under glacial and early interglacial climate conditions. Science 369, 1000–1005.

3. Xu, S., Das, S.K., and Archer, L.A. (2013). The Li-CO_2 battery: a novel method for CO_2 capture and utilization. RSC Advances 3, 6656.

4. Mu, X., Pan, H., He, P., and Zhou, H. (2020). Li-CO_2 and Na-CO_2 Batteries: Toward Greener and Sustainable Electrical Energy Storage. Adv. Mater. 32, e1903790.

5. Li, X., Yang, S., Feng, N., He, P., and Zhou, H. (2016). Progress in research on Li-CO_2 batteries: Mechanism, catalyst and performance. Chin. J. Catal. 37, 1016–1024.

6. Yang, S., He, P., and Zhou, H. (2016). Exploring the electrochemical reaction mechanism of carbonate oxidation in Li-air/CO_2 battery through tracing missing oxygen. Energy Environ. Sci. 9, 1650–1654.

7. Qiao, Y., Yi, J., Wu, S., Liu, Y., Yang, S., He, P., and Zhou, H. (2017). Li-CO_2 Electrochemistry: A New Strategy for CO_2 Fixation and Energy Storage. Joule 1, 359–370.

8. Xie, J., Zhou, Z., and Wang, Y. (2019). Metal-CO_2 Batteries at the Crossroad to Practical Energy Storage and CO_2 Recycle. Adv. Funct. Mater. 30, 1908285.

9. Chen, K., Huang, G., Ma, J.L., Wang, J., Yang, D.Y., Yang, X.Y., Yu, Y., and Zhang, X.B. (2020). The Stabilization Effect of CO_2 in Lithium-Oxygen/CO_2 Batteries. Angew. Chem. Int. Ed. Engl. 59, 16661–16667.

10. Li, J., Wang, L., Zhao, Y., Li, S., Fu, X., Wang, B., and Peng, H. (2020). Li-CO_2 Batteries Efficiently Working at Ultra-Low Temperatures. Adv. Funct. Mater. 30, 2001619.

11. Hu, A., Shu, C., Xu, C., Liang, R., Li, J., Zheng, R., Li, M., and Long, J. (2019). Design strategies toward catalytic materials and cathode structures for emerging Li-CO_2 batteries. J. Mater. Chem. A Mater. Energy Sustain. 7, 21605–21633.

12. Zhang, Z., Bai, W.-L., Wang, K.-X., and Chen, J.-S. (2020). Electrocatalyst design for aprotic Li-CO_2 batteries. Energy Environ. Sci. 13, 4717–4737.

13. Jiao, Y., Qin, J., Sari, H.M.K., Li, D., Li, X., and Sun, X. (2021). Recent progress and prospects of Li-CO_2 batteries: Mechanisms, catalysts and electrolytes. Energy Storage Mater. 34, 148–170.

14. Zhang, Z., Zhang, Q., Chen, Y., Bao, J., Zhou, X., Xie, Z., Wei, J., and Zhou, Z. (2015). The First Introduction of Graphene to Rechargeable Li-CO_2 Batteries. Angew. Chem. Int. Ed. Engl. 54, 6550–6553.

15. Zhang, X., Zhang, Q., Zhang, Z., Chen, Y., Xie, Z., Wei, J., and Zhou, Z. (2015). Rechargeable Li-CO_2 batteries with carbon nanotubes as air cathodes. Chem. Commun. (Camb.) 51, 14636–14639.

16. Li, X., Zhou, J., Zhang, J., Li, M., Bi, X., Liu, T., He, T., Cheng, J., Zhang, F., Li, Y., et al. (2019). Bamboo-Like Nitrogen-Doped Carbon Nanotube Forests as Durable Metal-Free Catalysts for Self-Powered Flexible Li-CO_2 Batteries. Adv. Mater. 31, e1903852.

17. Qie, L., Lin, Y., Connell, J.W., Xu, J., and Dai, L. (2017). Highly Rechargeable Lithium-CO_2 Batteries with a Boron- and Nitrogen-Codoped Holey-Graphene Cathode. Angew. Chem. Int. Ed. Engl. 56, 6970–6974.

18. Xu, S.-M., Ren, Z.-C., Liu, X., Liang, X., Wang, K.-X., and Chen, J.-S. (2018). Carbonate

decomposition: Low-overpotential Li-CO_2 battery based on interlayer-confined monodisperse catalyst. Energy Storage Mater. *15*, 291–298.

19. Yang, S., Qiao, Y., He, P., Liu, Y., Cheng, Z., Zhu, J.-j., and Zhou, H. (2017). A reversible lithium-CO_2 battery with Ru nanoparticles as a cathode catalyst. Energy Environ. Sci. *10*, 972–978.

20. Zhao, H., Li, D., Li, H., Tamirat, A.G., Song, X., Zhang, Z., Wang, Y., Guo, Z., Wang, L., and Feng, S. (2019). Ru nanosheet catalyst supported by three-dimensional nickel foam as a binder-free cathode for Li-CO_2 batteries. Electrochim. Acta *299*, 592–599.

21. Xing, Y., Yang, Y., Li, D., Luo, M., Chen, N., Ye, Y., Qian, J., Li, L., Yang, D., Wu, F., et al. (2018). Crumpled Ir Nanosheets Fully Covered on Porous Carbon Nanofibers for Long-Life Rechargeable Lithium-CO_2 Batteries. Adv. Mater. *30*, e1803124.

22. Zhang, B.W., Jiao, Y., Chao, D.L., Ye, C., Wang, Y.X., Davey, K., Liu, H.K., Dou, S.X., and Qiao, S.Z. (2019). Targeted Synergy between Adjacent Co Atoms on Graphene Oxide as an Efficient New Electrocatalyst for Li-CO_2 Batteries. Adv. Funct. Mater. *29*, 1904206.

23. Ma, W., Lu, S., Lei, X., Liu, X., and Ding, Y. (2018). Porous Mn_2O_3 cathode for highly durable Li-CO_2 batteries. J. Mater. Chem. A Mater. Energy Sustain. *6*, 20829–20835.

24. Li, S., Liu, Y., Zhou, J., Hong, S., Dong, Y., Wang, J., Gao, X., Qi, P., Han, Y., and Wang, B. (2019). Monodispersed MnO nanoparticles in graphene-an interconnected N-doped 3D carbon framework as a highly efficient gas cathode in Li-CO_2 batteries. Energy Environ. Sci. *12*, 1046–1054.

25. Yang, C., Guo, K., Yuan, D., Cheng, J., and Wang, B. (2020). Unraveling Reaction Mechanisms of Mo_2C as Cathode Catalyst in a Li-CO_2 Battery. J. Am. Chem. Soc. *142*, 6983–6990.

26. Li, S., Dong, Y., Zhou, J., Liu, Y., Wang, J., Gao, X., Han, Y., Qi, P., and Wang, B. (2018). Carbon dioxide in the cage: manganese metal–organic frameworks for high performance CO_2 electrodes in Li-CO_2 batteries. Energy Environ. Sci. *11*, 1318–1325.

27. Li, X., Wang, H., Chen, Z., Xu, H.S., Yu, W., Liu, C., Wang, X., Zhang, K., Xie, K., and Loh, K.P. (2019). Covalent-Organic-Framework-Based Li-CO_2 Batteries. Adv. Mater. *31*, e1905879.

28. Huang, S., Chen, D., Meng, C., Wang, S., Ren, S., Han, D., Xiao, M., Sun, L., and Meng, Y. (2019). CO_2 Nanoenrichment and Nanoconfinement in Cage of Imine Covalent Organic Frameworks for High-Performance CO_2 Cathodes in Li-CO_2 Batteries. Small *15*, e1904830.

29. Zhang, Y., Zhong, R.-L., Lu, M., Wang, J.-H., Jiang, C., Gao, G.-K., Dong, L.-Z., Chen, Y., Li, S.-L., and Lan, Y.-Q. (2021). Single Metal Site and Versatile Transfer Channel Merged into Covalent Organic Frameworks Facilitate High-Performance Li-CO_2 Batteries. ACS Cent. Sci. *7*, 175–182.

30. Zhang, Z., Yang, C., Wu, S., Wang, A., Zhao, L., Zhai, D., Ren, B., Cao, K., and Zhou, Z. (2019). Exploiting Synergistic Effect by Integrating Ruthenium-Copper Nanoparticles Highly Co-Dispersed on Graphene as Efficient Air Cathodes for Li-CO_2 Batteries. Adv. Energy Mater. *9*, 1802805.

31. Xing, Y., Wang, K., Li, N., Su, D., Wong, W.-T., Huang, B., and Guo, S. (2020). Ultrathin RuRh Alloy Nanosheets Enable High-Performance Lithium-CO_2 Battery. Matter *2*, 1494–1508.

32. Jin, Y., Chen, F., and Wang, J. (2020). Achieving Low Charge Overpotential in a Li-CO_2 Battery with Bimetallic RuCo Nanoalloy Decorated Carbon Nanofiber Cathodes. ACS Sustainable Chem. Eng. *8*, 2783–2792.

33. Tan, P., Wei, Z.H., Shyy, W., Zhao, T.S., and Zhu, X.B. (2016). A nano-structured RuO_2/NiO cathode enables the operation of non-aqueous lithium-air batteries in ambient air. Energy Environ. Sci. *9*, 1783–1793.

34. Du, Y., Liu, Y., Yang, S., Li, C., Cheng, Z., Qiu, F., He, P., and Zhou, H. (2021). A rechargeable all-solid-state Li-CO_2 battery using a $Li_{1.5}Al_{0.5}Ge_{1.5}(PO_4)_3$ ceramic electrolyte and nanoscale RuO_2 catalyst. J. Mater. Chem. A Mater. Energy Sustain. *9*, 9581–9585.

35. Ren, S., Joulié, D., Salvatore, D., Torbensen, K., Wang, M., Robert, M., and Berlinguette, C.P. (2019). Molecular electrocatalysts can mediate fast, selective CO_2 reduction in a flow cell. Science *365*, 367–369.

36. Linstead, R.P. (1953). Discoveries among conjugated macrocyclic compounds. J. Chem. Soc. *12*, 2873–2884.

37. Lim, R.J., Xie, M., Sk, M.A., Lee, J.-M., Fisher, A., Wang, X., and Lim, K.H. (2014). A review on the electrochemical reduction of CO_2 in fuel cells, metal electrodes and molecular catalysts. Catal. Today *233*, 169–180.

38. Liu, X., Meng, J., Zhu, J., Huang, M., Wen, B., Guo, R., and Mai, L. (2021). Comprehensive Understandings into Complete Reconstruction of Precatalysts: Synthesis, Applications, and Characterizations. Adv. Mater. *33*, e2007344.

39. Li, J., Zhao, H., Qi, H., Sun, X., Song, X., Guo, Z., Tamirat, A.G., Liu, J., Wang, L., and Feng, S. (2019). Drawing a Pencil-Trace Cathode for a High-Performance Polymer-Based Li-CO_2 Battery with Redox Mediator. Adv. Funct. Mater. *29*, 1806863.

40. Chen, J., Zou, K., Ding, P., Deng, J., Zha, C., Hu, Y., Zhao, X., Wu, J., Fan, J., and Li, Y. (2019). Conjugated Cobalt Polyphthalocyanine as the Elastic and Reprocessable Catalyst for Flexible Li-CO_2 Batteries. Adv. Mater. *31*, e1805484.

41. Wang, J., Gan, L., Zhang, Q., Reddu, V., Peng, Y., Liu, Z., Xia, X., Wang, C., and Wang, X. (2019). A Water-Soluble Cu Complex as Molecular Catalyst for Electrocatalytic CO_2 Reduction on Graphene-Based Electrodes. Adv. Energy Mater. *9*, 1803151.

42. Sun, L., Huang, Z., Reddu, V., Su, T., Fisher, A.C., and Wang, X. (2020). A Planar, Conjugated N_4-Macrocyclic Cobalt Complex for Heterogeneous Electrocatalytic CO_2 Reduction with High Activity. Angew. Chem. Int. Ed. Engl. *59*, 17104–17109.

43. Hu, X.M., Rønne, M.H., Pedersen, S.U., Skrydstrup, T., and Daasbjerg, K. (2017). Enhanced Catalytic Activity of Cobalt Porphyrin in CO_2 Electroreduction upon Immobilization on Carbon Materials. Angew. Chem. Int. Ed. Engl. *56*, 6468–6472.

44. Zhang, X., Wang, Y., Gu, M., Wang, M., Zhang, Z., Pan, W., Jiang, Z., Zheng, H., Lucero, M., Wang, H., et al. (2020). Molecular engineering of dispersed nickel phthalocyanines on carbon nanotubes for selective CO_2 reduction. Nat. Energy *5*, 684–692.

45. Shojiro, O. (1977). Preparation of macrocyclic compounds by thermal dimerization of 1,10-phenanthroline derivatives. J. Chem. Soc., Perkin Trans. 1 *2*, 214–216.

46. Zhu, J., Xia, L., Yang, W., Yu, R., Zhang, W., Luo, W., Dai, Y., Wei, W., Zhou, L., Zhao, Y., and Mai, L. (2021). Activating Inert Sites in Cobalt Silicate Hydroxides for Oxygen Evolution through Atomically Doping. Energy Environ. Mater. Published online May 24, 2021. https://doi.org/10.1002/EEM2.12219.

47. Yang, Q., Jia, Y., Wei, F., Zhuang, L., Yang, D., Liu, J., Wang, X., Lin, S., Yuan, P., and Yao, X. (2020). Understanding the Activity of Co-N_{4-x} C_x in Atomic Metal Catalysts for Oxygen Reduction Catalysis. Angew. Chem. Int. Ed. Engl. *59*, 6122–6127.

48. Pan, Y., Lin, R., Chen, Y., Liu, S., Zhu, W., Cao, X., Chen, W., Wu, K., Cheong, W.C., Wang, Y., et al. (2018). Design of Single-Atom Co-N_5 Catalytic Site: A Robust Electrocatalyst for CO_2 Reduction with Nearly 100% CO Selectivity and Remarkable Stability. J. Am. Chem. Soc. *140*, 4218–4221.

49. Yang, H., Wu, Y., Li, G., Lin, Q., Hu, Q., Zhang, Q., Liu, J., and He, C. (2019). Scalable Production of Efficient Single-Atom Copper Decorated Carbon Membranes for CO_2 Electroreduction to Methanol. J. Am. Chem. Soc. *141*, 12717–12723.

50. Zhao, Y., Wang, J., and Pei, R. (2020). Micron-Sized Ultrathin Metal-Organic Framework Sheet. J. Am. Chem. Soc. *142*, 10331–10336.

51. Zhu, J., Li, S., Zhuang, Z., Gao, S., Hong, X., Pan, X., Yu, R., Zhou, L., Moskaleva, L.V., and Mai, L. (2021). Ultrathin Metal Silicate Hydroxide Nanosheets with Moderate Metal–Oxygen Covalency Enables Efficient Oxygen Evolution. Energy Environ. Mater. Published online December 13, 2021. https://doi.org/10.1002/eem2.12155.

52. Li, Z., Ye, R., Feng, R., Kang, Y., Zhu, X., Tour, J.M., and Fang, Z. (2015). Graphene Quantum Dots Doping of MoS_2 Monolayers. Adv. Mater. *27*, 5235–5240.

53. Shi, R., Liu, L., Lu, Y., Li, Y., Zheng, S., Yan, Z., Zhang, K., and Chen, J. (2020). In Situ Polymerized Conjugated Poly(pyrene-4,5,9,10-tetraone)/Carbon Nanotubes Composites for High-Performance Cathode of Sodium Batteries. Adv. Energy Mater. *11*, 2002917.